



Mine tailing extraction indexes and model using remote-sensing images in southeast Hubei Province

Lina Hao¹ · Zhi Zhang² · Xiaoxia Yang¹

Received: 22 July 2018 / Accepted: 8 July 2019 / Published online: 2 August 2019
© The Author(s) 2019

Abstract

Southeast Hubei province is an important iron–copper production base in China, which has produced a large number of mine tailings from mining activities. Although they contain a certain amount of iron or copper as secondary mineral resources, the mine tailings and related acid wastewater can lead to environmental pollution through sand blowing or seepage. For effective resource utilization and environmentally conscious development, rapid evaluations of the spatial distribution, type, and age of mine tailings are of national importance. Using spectral features, which are determined by the structure and composition of tailings, we develop an all-band tailing index, a modified normalized difference tailing index (MNTI), and a normalized difference tailings index for Fe-bearing minerals (NDTIFe). The all-band tailings index reflect the micro-structure and overall high reflectivity of mine tailings by comprehensively utilizing information from each band of Landsat 8 data. The MNTI and NDTIFe provide enhanced tailings composition information from the perspective of anion (carbanion and hydroxy) and cation (mainly ferric ion) contents, respectively. A tailing extraction model (TEM) is built using these three indexes to extract mine tailing information in Huangshi city. The TEM proposed in this paper can successfully and rapidly extract mine tailings information with an extraction precision of 84% in the research area.

Keywords All-band mine tailing index · Modified normalized difference tailing index · Normalized difference tailing index for Fe-bearing minerals · Tailing extraction model

Introduction

In recent years, lasting environmental problems caused by the exploitation of mineral resources, such as abandoned open mining pits, dumps, and tailing pools, are attracting increasing scientific concern. Mining-related environmental problems are clearly illustrated by surface landscape destruction, land form changes, ecological degradation, heavy metal pollution of soils, and water body pollution (Chevrel et al. 2002). Specifically, secondary Fe-bearing mineral oxides and acidic mine drainage water left behind by mining activities have resulted in vegetation, soil, and water pollution. Remote-sensing technology can be used to

monitor mine environmental problems by monitoring the open mining pit, waste dumps, tail sands, weathering and oxidation processes, oxidation products (mainly secondary iron oxides), and pollution of the acidic mining waste water.

Remote-sensing image is a commonly tool in mining pollution research. Popular methods of identifying mining pollution are based on imaging spectrum technology (Shang et al. 2009; Swayze et al. 2000; Rianza and Müller 2010; Ferrier 1999; Choe et al. 2008; Mars and Crowley 2003; Raj et al. 2015), non-imaging spectrum technology (Irene et al. 2005), multispectral technology (Ciampalini et al. 2013; Morais 2012; Dogan 2008, 2009; Elsayed Zeinelabdein and Albiely 2008; Schimmer 2008), etc. Research shows that the spectral features of secondary iron oxide lie between the visible and near-infrared band (0.43–1.3 μm) and exhibit strong reflection in the red band and strong absorption in the near-infrared, blue, and green bands (Skulte et al. 2018; Wang et al. 2011). The spectral features of the secondary pollutants of carbonate and hydroxyl minerals lie in short-wave-infrared wavelengths (1.9–2.4 μm) and exhibit weak absorption near 2.3 μm . The visible–near-infrared spectrum

✉ Lina Hao
hao_ln@qq.com

¹ State Key Laboratory of Geohazard Prevention and Geoenvironment Protection, Faculty of Earth Sciences, Chengdu University of Technology, Chengdu 610059, China

² Institute of Geophysics and Geomatics, China University of Geosciences, Wuhan 430074, China

based on the multispectral remote-sensing technique is often utilized to extract the iron oxide information of hematite, magnetite, and goethite minerals. Commonly used remote-sensing image enhancement methods include the ratio method (Madani 2009; Ducart et al. 2016), principal component transformation method (Shalaby et al. 2010), false color composite method (Dehnavi et al. 2010), and decorrelation stretch of HIS method (Al Rawashdeh et al. 2006).

This research analyzes the spectral characteristics of mine tailings sand based on its structure and composition. We used the principal component transform method and the ratio method to enhance the high reflection spectral characteristics, which reflect tailings sand structural features, and the absorption–reflection spectral characteristics, respectively. The aim of this paper is to extract mine tailings pond quickly and automatically by the spectral figure of the tailings from remote-sensing images.

Study area and research data

Study area

Southeast Hubei, China, has a northern subtropical monsoon climate, which is warm and wet, with abundant rainfall, and a substantial number of natural water bodies, such as rivers, lakes, and ponds. Formation of metallic ore deposits in the area is mostly related to volcanic activity. These ore deposits are typical Skarn-type deposits controlled by carbonates (Guo et al. 2011) and are relatively concentrated in Tieshan, Tonglvshan, Jinshandian, Lingxiang, Tongshankou, Jilongshan, and Fengshan. The area is the traditional production base of iron and copper in China, with relatively concentrated ore fields comprising medium to small-scale ore deposits. The area has a 50-year exploitation history of modern mining and ore-processing (Liu et al. 2010), which has resulted in more than 500 tailings of various sizes in the region (Liu et al. 2009a, b). Although we did not investigate the specific location, area, storage capacity, and major source minerals of each tailing pond, ore dressing and smelting activities are generally performed nearby due to cost saving reasons; thus, the distribution of tailing ponds formed by dressing and smelting processes typically correlates well with the exploitation location of ore resources.

Huangshi city in Hubei Province was chosen as the study area, which is a well-known resource-based city in China (Fig. 1) and is located at 29°31' to 30°19'N and 114°30' to 115°30'E. The landforms around Huangshi consist of low mountains, hills and basins, with the lowest elevation of 8.7 m and a highest of 862 m. This city contains both natural vegetation and artificial vegetation. Natural vegetation includes subtropical evergreen broad-leaved forest and mixed evergreen and deciduous broad-leaved forest, with a

few regions of broad-leaved deciduous forest, subtropical coniferous forest, and bushwood; artificial vegetation contains mainly of rice and vegetable fields. The city, which is famous for its iron resources, also has many iron ore mines that have produced a large number of open pits, solid-waste dumps, and a series of tailing ponds. Tailing ponds cause the most serious environmental pollution; tailings and acidic mine waste water in the ponds continually pollute the surroundings through sand blowing or seepage. After the tailing ponds were abandoned, the dried tailings were typically transported inshore or to higher ground due to gradual evaporation of water content. In bad weather, such as strong wind, pollutants such as metal ion and dust are transported large distances in the air (Fig. 2a).

In recent years, the demand for ore resources has increased rapidly along with economic development; consequently, a number of small ore dressing industries have appeared in the study area (Fig. 2b, c). In general, such industries discharge their tailings directly into nearby ponds or low-lying areas. Such tailing ponds have very poor facilities without no impermeable layer (Fig. 2d) allowing acidic mine waste water to continuously diffuse into the surrounding environment by seepage. Therefore, the rapid and accurate identification and location of tailing ponds in remote-sensing images is key for environmental evaluations, environment management, and the secondary development and application of resources.

Data

To extract mine tailing information in the study area, we produced a tailing extraction model using Landsat-8 OLI images obtained from USGS. The Landsat-8 OLI images were acquired on October 15, 2014, with a medium spatial resolution of 30 m. In the study, we used the blue, green, red, near-infrared (NIR), shortwave-infrared (SWIR) 1, and SWIR 2 spectral bands which cover the visible–near-infrared and shortwave-infrared spectral range. Pre-processing, including radiation correction and geometric correction, was performed using ENVI 5.3 and ERDAS 2016 (Xu and Tang 2013).

Composition and structure of tailings

Compositional features of tailings

The composition of the tailings in the study area is shown in Table 1. The metallic mineral content is 9–10% and the SiO₂ content is 30–40%, which mainly exists in the form of iron oxides and rock debris. The major metallic minerals in the tails include pyrite, hematite, magnetite, and siderite. The main non-metallic mineral is quartz; silicate minerals such

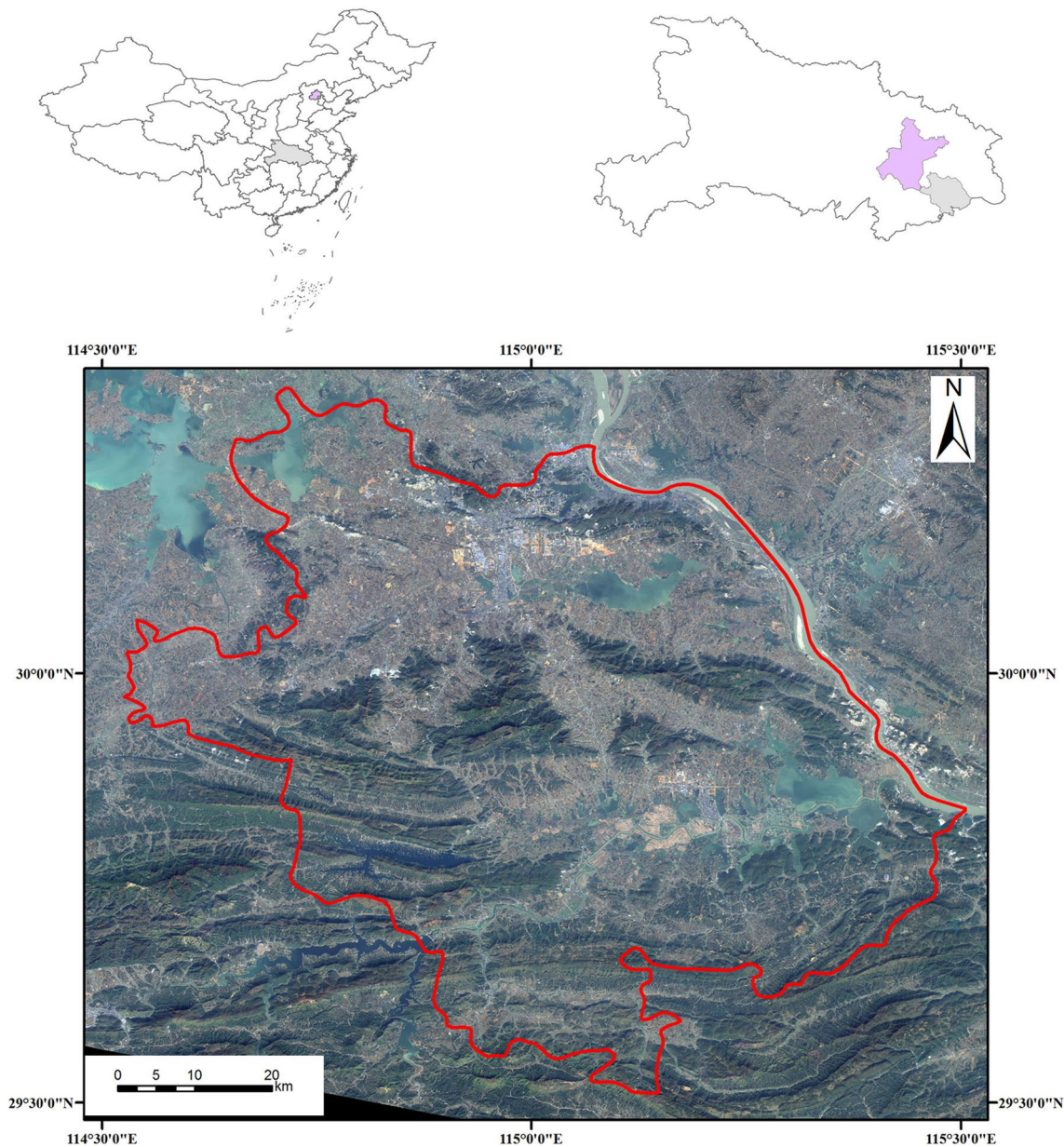


Fig. 1 Geographical location of the study area and tailing characteristics.(image color composite using red, green, and blue bands based on Landsat 8 data)

as anorthose and potassium feldspar and a small amount of carbonate minerals such as calcite and dolomite also exist. The tailings sand is rust red on a true-color remote-sensing image (Fig. 3).

Structural features of tailings sand

After the crude ore is crushed and ground during dressing and smelting processes, the grain size reaches the mm or μm scale. Grains below 0.074 mm account for 70–90% of all tailings particles, and the weighted average grain size

is approximately 0.03–0.05 mm (Hong and Kong 2003). Because of the fine grain size, a substantial amount of tailings sand exists in the form of suspended particles. Tailings particles are either in the dried, slurry, or solution state according to their composition and evaporation periods (Fig. 4). The reflectivity of dry tailings sand is higher than that of mud tailings sand, which contains a small amount of water, but the overall reflectivity is typically low. On a remote-sensing image, the color of dry tailing sand is bright and the color of slurry tailing sand is dark. As the water reflectance decreases with increasing wavelength in the



Fig. 2 Examples of simple and crude tailing ponds

Table 1 Major composition of iron ore tailings in the study area

Sample name	Original no.	Indoor no.	Cu	Zn	Pb	TFe	SiO ₂
Iron tail sand	Fe-1	A124030001	532.5	149.4	25.73	9.53	32.59
Iron tail sand	Fe-2	A124030002	655.7	140.75	20.3	9.88	38.32

Unit of measurement: Cu–Pb: $\mu\text{g/g}$, TFe–SiO₂ %; (tailings composition determined by the Wuhan Mineral Resources Supervision and Testing Center of the Ministry of Land and Resources)

visible–near-infrared–shortwave-infrared region, the slurry tailings sand reflectance decreases compared to that of dry tailings sand. The reflectance of slurry tailings sand is similar to that of dry tailings sand in the visible–near-infrared region; however, it is 7.5% lower in the shortwave-infrared range, as is shown in Fig. 5.

Spectral characteristics of tailings and other background features

High reflection characteristics

The fine-grained structural features indicate that tailings have relatively high reflectivity in the visible and near-infrared

bands (Baranoski et al. 2014). When the volume is constant, the reflection or absorption of solar radiation energy by a ground object depends on its size (Schimmer 2008). A larger object will absorb solar radiation due to a relatively long inner light path, resulting in a decrease of reflectivity; while a smaller object will reflect more solar radiation due to a larger surface area, resulting in an increase of reflectivity. Therefore, the ratio between the superficial area and the volume of the ground object is an important factor determining the solar radiation reflected by a ground object. Extremely small grain is a significant feature of tailings, i.e., the ratio between superficial area and volume is very large. This characteristic greatly enhances the ability of tailings to reflect solar radiation, resulting in their relatively high observed reflectivity.

Fig. 3 Rust red color of tailing sand on a true-color remote-sensing image

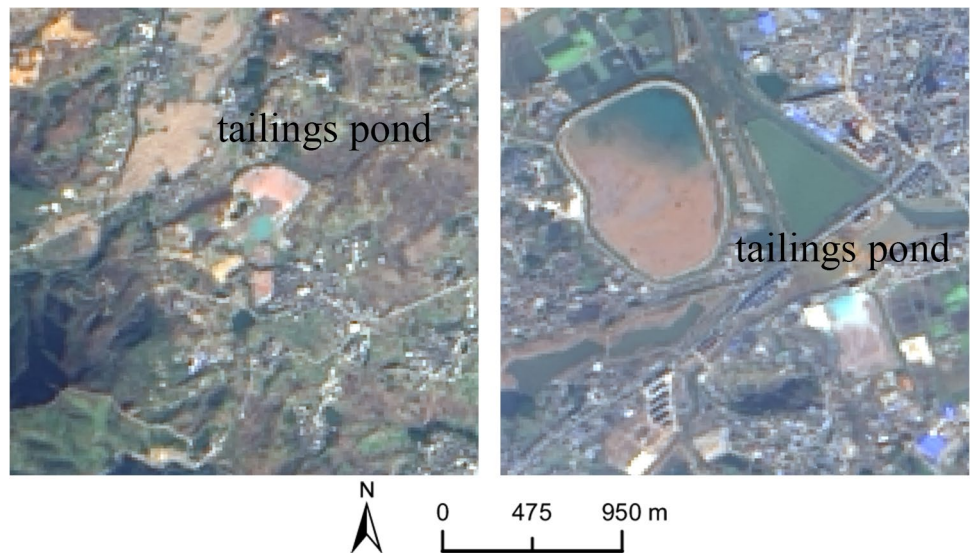
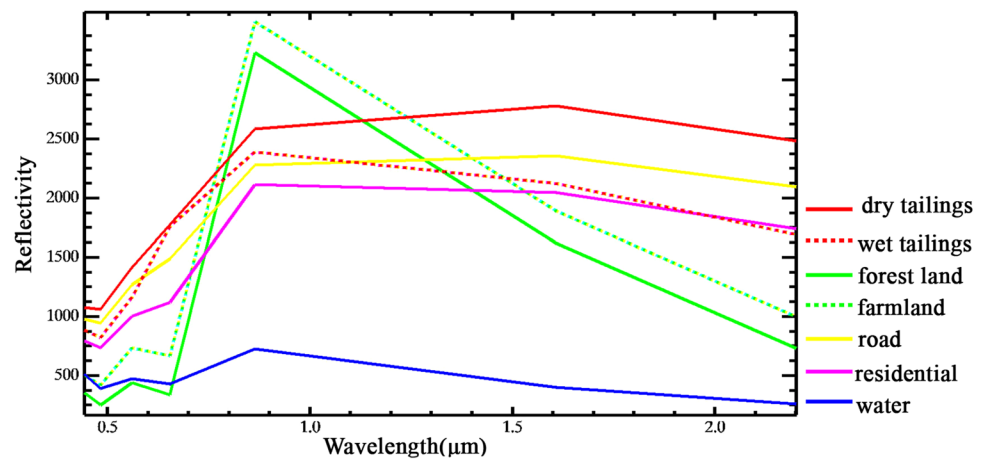


Fig. 4 Tailings sand showing the range of exit forms in ponds: **a** slurry; **b** solution; and **c** dried

Fig. 5 Spectral curves for typical surface features in the Landsat 8 image



Spectral features of anions group in tailings sand

The anion group contained in tailings has spectral features which are predominantly CO_3^{2-} ion and OH^- ions.

Carbonate ion spectra mainly range from 2.33–2.37 to 2.52–2.57 μm (equivalent to the Landsat-8 SWIR 2), and indicate strong absorption, e.g., the absorption band of siderite is 2.35 μm and 2.56 μm . The spectral absorption

characteristics of OH^- are mainly due to stretching vibration. The specific absorption location is related to the OH^- -linked metal ions. For example, minerals containing Fe–OH groups have clear absorption characteristics (e.g., jarosite) at 2.24–2.30 μm (equivalent to the Landsat-8 SWIR 2) (Mazhari et al. 2017). Therefore, the shortwave-infrared band from Landsat-8 images can be used to enhance tailings sand information related to anion content.

Spectral features of cations in tailing sand

The cations contained in tailings have spectral features which are predominantly Fe^{3+} ions, which have distinct characteristic bands in the visible–near-infrared–shortwave-infrared wavelengths (approximately 0.45–2.35 μm); absorption characteristics are exhibited in blue, green, and near-infrared bands, and reflection characteristics are exhibited in red and shortwave-infrared bands. Based on the measured iron oxides in the tailings sand and the specific characteristics of the Landsat-8 image, the iron oxides have two distinct absorption bands and reflection peaks in the Landsat-8 spectral wavelength range. The first absorption site is located at 0.52–0.60 μm (equivalent to the Landsat-8 green band), the second absorption site is located at 0.8–1.0 μm (equivalent to the Landsat-8 near-infrared band), while the reflection peaks are located at 0.63–0.69 μm (equivalent to the Landsat-8 red band) and 1.55–1.75 μm (equivalent to the Landsat-8 SWIR 1). In conclusion, in the spectral region of the Landsat-8 image, there are two bimodal spectral features with relatively high reflectance values, so the visible and near-infrared–shortwave-infrared bands of the Landsat-8 image can be used to enhance tailings sand information related to cation content.

Spectral characteristics of the other features in the image

The surface features in the study area predominantly include tailings, vegetation, residential buildings, natural water bodies, and roads. To analyze the spectral features of these objects, 350 samples of dry and wet tailings, forest, farmland, road, residential buildings, and water bodies were randomly selected, and a spectrum curve was formed for each category using statistics from 50 samples (Fig. 5). The reflectance of dry tailings in the Landsat-8 OLI images after atmospheric correction is the highest in visible-to-shortwave-infrared wavelengths, while that of wet tailings is slightly lower, but far higher than that of natural water bodies. In the visible wave band, the reflectivity of all ground objects except natural water bodies increases with increasing wavelength. The reflectivity of the dry and wet tailings increases more rapidly, i.e., the slope of the spectral curves is larger. The reflectivity of vegetation and residential areas

exhibits weak absorption in the red band, so the slope of the spectrum curve in the visible wave band range is small. In the near-infrared–shortwave-infrared wavelength range, the reflectivity of all features decreases with increasing wavelength except for dry tailings, whose reflectivity increases slightly (due to the combined action of the ferric iron and carbonate ions in the dry tailings sand). The rate of vegetation reduction is highest, followed by roads, residential areas, wet tailings, and water bodies. The spectral characteristics in the visible, near-infrared, shortwave-infrared bands are recognizable for all ground objects in the study area. Due to tailings' structure and components of its major anionic and cationic, a tailing sand index can be established by the visible–near-infrared and shortwave-infrared spectral characteristics using Landsat-8 image.

Tailing sand indexes and extraction model

All-band tailing index

The all-band tailing index is based on all wave bands of the Landsat-8 image. Through a principal component analysis (PCA) of Landsat-8 images, we choose the principal component that can best highlight the spectral characteristics of the tailings to extract their information. PCA is a powerful tool for enhancement all bands of Landsat-8 and reducing correlation and redundancy (Mazhari et al. 2017).

The transform module of ENVI 5.3 was used to perform the principal component analysis. The results of the principal component analysis of the blue, green, red, near-infrared, SWIR 1, and SWIR 2 of Landsat-8 OLI images are shown in Table 2. Of the six principal components, PC5 components are used to extract tailing sand information using comprehensive information for each band of the Landsat-8 OLI images. If appropriate threshold values are set for PC5, tailings sand with other features can be effectively separated.

Modified normalized difference tailings sand index in the near-infrared–shortwave-infrared spectral band

In the Landsat-8 near-infrared–shortwave-infrared spectrum, the reflectance of dry tailings sand increases slightly with increasing wavelength, while that of other objects decreases, and the reflectance of vegetation decreases the fastest. In the near-infrared band, the reflectivity of vegetation is much higher than that of tailings sand and other features; however, when the wavelength is longer than 1.4 μm , the reflectivity of vegetation is lower than that of tailings, roads, residential areas, etc., and only higher than that of water. To enhance the spectral difference between tailings and other objects, a Modified Normalized Difference Tailings Index (MNDTI) is

Table 2 Principal component characteristics after PC transform

Characteristics of the principal components	Blue band	Green band	Red band	Near-infrared band	Shortwave-infrared band 1	Shortwave-infrared band 2
PC1	- 0.16184	- 0.24489	- 0.34283	- 0.3615	- 0.607711	- 0.544345
PC2	0.16627	0.158008	0.284183	- 0.87295	- 0.036795	0.321304
PC3	- 0.32667	- 0.46242	- 0.53228	- 0.25946	0.52837	0.222814
PC4	0.163707	- 0.03523	- 0.39717	0.176539	- 0.538989	0.70181
PC5	- 0.70345	- 0.31947	0.52884	0.078961	- 0.244169	0.239953
PC6	- 0.56374	0.773263	- 0.28456	- 0.0506	0.005596	0.026307

proposed based on Landsat-8 OLI images of near-infrared and shortwave-infrared spectral bands, as shown in formula 1:

$$\text{MNDTI} = (\text{NIR} - \text{SWIR2}) / (\text{NIR} + \text{SWIR2}) * c, \quad (1)$$

where c is a constant used to expand the gray value range of MNDTI and enhance the amount of quantitative information.

Normalized difference iron stain index of tailings sand in the visible spectral band

The main metal component of the tailings is iron, which is rust red in the simulated true-color remote-sensing images due to oxidation of the iron (Fig. 3). The mechanism of extracting iron stain information from remote-sensing images is based on the spectral response characteristics of ferric ions in the visible and near-infrared regions. The specific reflections of ferric ions in the red band (0.63–0.69 μm) are high, while those in the blue band (0.45–0.52 μm), green band (0.52–0.62 μm), and near-infrared band (0.76–0.90 μm) are low with stronger absorption. In Fig. 5, the spectral characteristics of typical features in the study area are significant in the visible–near-infrared region of the Landsat-8 OLI images, and the reflectivity spectral curves of all objects show an increasing trend with increasing wavelength. However, the rate of increase differs; that is, the slope of the spectral curve is different. The slope of the reflectance spectral curve for dry and wet tailings sand is greatest in the visible–near-infrared region. The reflectivity of vegetation changes the least in the visible region (green peak–red valley); however, it increases most rapidly in the red–near-infrared region, i.e., the maximum slope of the reflectivity curve is located in the red and near-infrared range. The slope of the reflectivity curve for residential areas and roads is smaller, while that of water bodies is the smallest. Therefore, to enhance tailings information, we used the red band and blue band of Landsat-8 to establish the NDTIFe (normalized difference tailings index of Fe-bearing minerals) based on the spectral characteristics of trivalent iron ions. The NDTIFe index is shown in formula (2):

$$\text{NDTIFe} = (\text{RED} - \text{BLUE}) / (\text{RED} + \text{BLUE}) * c, \quad (2)$$

where c is a constant used to expand the gray value range of the NDTIFe and enhance the amount of quantitative information.

Tailing sand extraction model

The all-band tailing sand index enhanced tailings sand and water body information in the whole spectral range of Landsat-8 OLI images for the visible–near-infrared–shortwave-infrared band, the MNDTI index enhanced anion information (carbonic ion and hydroxy information) of tailing sand in the near-infrared–shortwave-infrared region, and the NDTIFe index enhanced cationic information (iron-stained information) in the visible band region. All three indexes enhanced tailing sand information in different ways by increasing the spectral difference between tailings sand and other background objects. By setting appropriate field values for the above indexes, a tailings extraction model (TEM) was established, as shown in formula (3):

$$\text{TEM} = (k1 < \text{PC5} < k2) \text{ and } (k3 < \text{MNDTI} < k4) \text{ and } (k5 < \text{NDTIFe} < k6), \quad (3)$$

where $k1$, $k2$, $k3$, $k4$, $k5$, and $k6$ are all constants, which can be set to a unified threshold in the same study area according to ground object and image features.

Experiments and results

To verify the effectiveness of the proposed TEM, we use the tailings shown in Fig. 1 as a typical sample area to calculate the eigenvalues for PC5, MNDTI, and NDTIFe. When calculating MNDTI and NDTIFe, c is 1000. Table 3 shows the statistical values of all types of feature samples. In Table 3, the mean PC5 values for wet tailings and water bodies are approximately 232.130 and - 38.895, respectively, and those of other ground objects are shown in Table 3. There is no overlap between the characteristic values of woodland, farmland, residential areas, roads, etc.

As a result, we can use PC5 to identify wet tailing sand. The NDTIFe index is better for identifying dry tailings sand, because they have a value near 392.399 and there is no overlap between the feature values of woodland, farmland, residential area, roads, and water bodies. The characteristic mean values of MNDTI for dry tailings sand samples are approximately 330.92 with minimal overlap from the other features such as forest land, cultivated land, residential areas, and roads. The characteristics mean values of MNDTI for wet tailings sand samples are around 261.633, and also show minimal overlap with other features such as forest land, cultivated land, residential areas, roads, and water bodies. Thus, MNDTI can be used as a supplementary index to extract tailings sand information.

Information related to the tailings reservoir around Yangxin rock was extracted using the statistical characteristics and experimental results of the study area, where k_1 , k_2 , k_3 , k_4 , k_5 , and k_6 were 125, 359, 200, 265, 330, and 455, respectively. Given the mixture of pixels of the Landsat-8 multispectral image with a resolution of 30 m, the extraction results of a single pixel were abandoned, and the final result is shown in Fig. 6.

By combining the Google Earth high-resolution image with actual field survey data, 25 tailings were randomly chosen to verify the TEM. The results show that 21 tailing reservoirs are correctly extracted, with only four incorrectly extracted reservoirs; therefore, the extraction accuracy of the tailings is approximately 84%. Of the four misjudged tailings, one is an open pit, one is a solid-waste heap, which both have similar reflectivity and spectral curves to the tailings, and the other two are engineering activities operations with higher reflectivity.

Discussion

In this study, Landsat-8 OLI remote-sensing images were used to swiftly find and locate tailings ponds in the study area based on the spectral features of different components

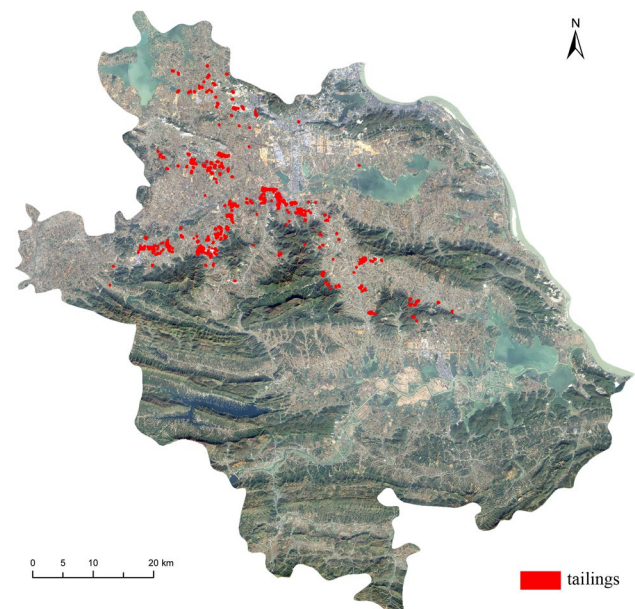


Fig. 6 Tailings extraction model results for Yangxin Rock

of the tailings and other ground objects. In remote-sensing images, the differences in the spectral features between tailings and other ground objects were derived from differences in their structures and components. Therefore, an enhanced image analysis was performed on these aspects.

Based on PCA analysis, considering the spectral characteristics of tailings sand and other objects and their response characteristics in the Landsat-8 OLI image, PC5 is chosen as all-band tailing index for the following reasons. (1) The principal component factor loading of the near-infrared band should be as low as possible to effectively enhance tailings sand information and restrict vegetation information. This is because the reflectance of tailings in the near-infrared band of Landsat-8 OLI images is lower than that of vegetation, but higher than the reflectance of vegetation and other objects in other bands. (2) The principal component factor loading of the red band should be high to effectively

Table 3 Statistical values of different feature samples

Tails index	Statistics	Dry tailings	Wet tailings	Woodland	Farmland	Residential area	Road	Water
PC5	MIN	-160.219	125.003	-10.709	-52.967	-106.191	-128.858	-59.238
	MAX	146.812	358.802	78.863	104.026	92.205	53.510	-20.108
	Mean	7.806704	232.130	29.224	20.612	-16.404	-34.138	-38.895
MNDTI	MIN	196.634	51.517	492.017	403.459	-74.935	-39.748	2.205
	MAX	515.24	593.085	685.792	647.086	376.559	233.905	662.338
	Mean	330.125	261.633	632.562	556.031	98.773	42.36	509.893
NDTIFe	MIN	330.92	0	80.189	128.991	103.081	179.416	-18.568
	MAX	454.61	289.855	211.409	294.729	282.387	271.118	179.924
	Mean	392.399	175.48	150.088	219.948	204.149	222.343	44.71

enhance the ferric contamination information of tailings sand, because the reflectance of ferric ions in the tailings sand is higher in the red band. (3) The principal component factor loading of SWIR 2 should be high to effectively enhance the carbonate ions information of tailings sand. This is because there is stronger absorption in SWIR 2 due to the composition of carbonate ions. (4) While ensuring that the characteristic principal components satisfy the first three conditions, the red band should represent the positive load, and the blue, green, and shortwave-infrared bands should represent the negative loads, which correspond to the relevant reflection and absorption characteristics of the tailings sand components. The principal component analysis showed that all-band tailing indexes using PC5 had enhanced the high reflection features resulted in the structures of tailings while simultaneously considering the spectral characteristics resulted in tailings components.

MNDTI enhanced the spectral information of carbonates group using NIR and SWIR 2 band, as the spectral diagnostic absorption features are in the shortwave-infrared bands (Bedini 2009; Baissa et al. 2011; Mazhari et al. 2017). The MNDTI index is improved from NDWI (Mcfeeters 1996) and MNDWI (Xu 2005) water body information extraction indexes, which effectively extract tailings sand information and can be used for tailings containing minimal water. The MNDWI index was based on McFeeters's NDWI index and fully considers the sharp reflectivity increase in the near-infrared-to-shortwave-infrared spectral wavelength of buildings; therefore, it uses SWIR 1 (TM/ETM⁺ band 5) instead of the near-infrared band used by the NDWI index. The MNDWI index was modified based on the spectral characteristics difference in the visible, near-infrared, and shortwave-infrared spectral wavelengths between tailing sand and other ground objects in the study area. While the reflectivity of features such as vegetation and water bodies decreases more rapidly in shortwave-infrared bands, which of the tailings changes slightly in the same bands, therefore, SWIR 2 is selected instead of SWIR 1, which is used in the MNDWI index. The MNDTI index can effectively inhibit information related to vegetation, water bodies, and buildings, while enhancing that related to tailings. Furthermore, to distinguish MNDTI from the normalized tailings index proposed by Schimmer (2008), our tailings index constructed in the near-infrared–shortwave-infrared region is referred to as the improved model. The normalization tailings index proposed by Schimmer mainly utilizes the characteristics of no vegetation growth on the surface of the tailings reservoir, which is based on the normalized vegetation index, only using the near-infrared and red band of the TM image. However, the modified normalized tailings index (MNDTI) takes full advantage of the spectral characteristics of tailing sand composition in the near-infrared–shortwave-infrared bands, which is sensitive to the identification of water features, such

as water bodies, wetlands, tailing sand, and other objects such as vegetation and buildings.

NDTIFe enhanced the spectral information of Fe³⁺-bearing minerals using visible bands, as the spectral diagnostic absorption features of Fe³⁺-bearing minerals are in visible–near-infrared wave bands (Zabcic et al. 2014; Jakob et al. 2016; Mazhari et al. 2017), NDTIFe is based on visible bands. Ultimately, the blue band is selected to establish the NDTIFe in the three strong absorption bands (blue, green, and near-infrared) for the following two reasons. (1) The MNDTI index is established based on the near-infrared band and SWIR 2; therefore, to make full use of the spectral information of Landsat-8 images, the NDTIFe index ignores the near-infrared band to avoid information redundancy. (2) The NDTIFe index chooses the blue band and discards the green band, which can effectively restrict vegetation and road information while enhancing the spectral differences between tailings sand, water bodies, and residential areas. NDTIFe index is sensitive to the identification of Fe³⁺-bearing minerals.

Combining the three indexes, the TEM was established to acquire tailing information in Huangshi City using Landsat-8 OLI images. The tailing pond extraction method proposed in this study is a time- and money-saving tool when compared to conventional geological mapping techniques (Mezned et al. 2016; Mazhari et al. 2017). In addition, Landsat-8 OLI images are free, compared to expensive hyperspectral data (Murphy and Monteiro 2013; Zabcic et al. 2014) and high spatial resolution data (Mezned et al. 2016).

However, we did not extract all the tailings in Huangshi City. As the resolution of the Landsat-8 multispectral images is only 30 m, very small tailings cannot be effectively extracted. Furthermore, the silicate contained in tailings cannot be extracted. The spectral features of silicate are in the thermal infrared wave bands (Matar and Bamousa 2013; Pour et al. 2017); however, the resolution of these bands of Landsat-8 is 100 m, which is much bigger than tailings in the study area. The next step in our research will explore how to combine hyperspectral images with high spatial resolution images to extract small-scale tailing reservoirs and study the response of soil and vegetation after water seepage of tailing reservoirs.

Conclusion

A tailing extraction model (TEM) was established by combining the all-band tailing sand index (mainly PC5), the MNDTI index, and the NDTIFe index. Compared with NDTI, the TEM fully considers iron stain, carbonate ion, and water information of the tailing sand, which are all important components. The TEM increases tailings information whilst

effectively restricting vegetation information by enhancing the reflectivity differences between tailings sand and water bodies, buildings, roads, and other major features. The TEM can rapidly and effectively locate a tailings pond in south-east Hubei province, providing accurate data support for the rational exploitation and utilization of mineral resources, as well as for monitoring and management of the ecological environment in mining areas.

Acknowledgements This work was supported by National Natural Science Foundation of China under Grants 41702358, 41771444, 41790445, 41630640; China Postdoctoral Science Foundation under Grant 2017M622982; key projects of Education Department of Sichuan Province under Grant 16ZA0090.

Open Access This article is distributed under the terms of the Creative Commons Attribution 4.0 International License (<http://creativecommons.org/licenses/by/4.0/>), which permits unrestricted use, distribution, and reproduction in any medium, provided you give appropriate credit to the original author(s) and the source, provide a link to the Creative Commons license, and indicate if changes were made.

References

- Al Rawashdeh S, Bassam S, Hamzah M (2006) The use of remote sensing technology in geological investigation and mineral detection in El Azraq-Jordan. *Cybergeo Eur J Geog Syst Model Geostats* 2856:203–219
- Baissa R, Labbassi K, Launeau P, Gaudin A, Ouajhain B (2011) Using HySpex SWIR-320m hyperspectral data for the identification and mapping of minerals in hand specimens of carbonate rocks from the Ankloute Formation (Agadir Basin, Western Morocco). *J Afr Earth Sci* 61:1–9
- Baranoski GVG, Kimmel BW, Chen TF, Miranda E (2014) Influence of sand-grain morphology and iron-oxide distribution patterns on the visible and near-infrared reflectance of sand-textured soils. *IEEE J Select Topics Appl Earth Obs Remote Sens* 7:3755–3763
- Bedini E (2009) Mapping lithology of the Sarfartoq carbonatite complex, southern West Greenland, using HyMap imaging spectrometer data. *Remote Sens Environ* 113:1208–1219
- Chevrel S, Belocky R, Grösel K (2002) Monitoring and assessing the environmental impact of mining activities in Europe using most advanced Earth observation techniques-MINEO, First results of the Alpine test site. In: *Environmental communication in the information society*, 16th conference, Wien, pp 519–526
- Choe E, Meer FVD, Ruitenbeek FV, Werff HVD, Smeth BD, Kim KW (2008) Mapping of heavy metal pollution in stream sediments using combined geochemistry, field spectroscopy, and hyperspectral remote sensing: a case study of the Rodalquilar mining area, SE Spain. *Remote Sens Environ* 112:3222–3233
- Ciampalini A, Garfagnoli F, Antonielli B, Moretti S, Righini G (2013) Remote sensing techniques using Landsat ETM plus applied to the; detection of iron ore deposits in Western Africa. *Arab J Geosci* 6:4529–4546
- Dehnavi AG, Sarikhani R, Nagaraju D (2010) Image processing and analysis of mapping alteration zones in environmental research, East of Kurdistan. *Iran World Appl Sci J* 11:278–283
- Dogan HM (2008) Applications of remote sensing and geographic information systems to assess ferrous minerals and iron oxide of Tokat province in Turkey. *Int J Remote Sens* 29:221–233
- Dogan HM (2009) Mineral composite assessment of Kelkit River Basin in Turkey by means of remote sensing. *J Earth Syst Sci* 118:701–710
- Ducart DF, Silva AM, Toledo CLB, Assis LMD, Ducart DF, Silva AM, Toledo CLB, Assis LMD (2016) Mapping iron oxides with Landsat-8/OLI and EO-1/hyperion imagery from the Serra Norte iron deposits in the Carajás Mineral Province, Brazil. *Braz J Geol* 46:331–349
- Elsayed Zeinelabdein KA, Albiely AI (2008) Ratio image processing techniques: a prospecting tool for mineral deposits, Red Sea Hills, NE Sudan. *Int Arch Photogramm Remote Sens Spat Inf Sci* 37:1295–1298
- Ferrier G (1999) Application of imaging spectrometer data in identifying environmental pollution caused by mining at Rodaquilar, Spain. *Remote Sens Environ* 68:125–137
- Guo Y, Bao ZY, Deng YM, Ma ZZ, Yan S (2011) Environmental geochemistry of abandoned flotation tailing reservoir from the Tonglvshan Fe–Cu sulfide mine in Daye, Central China. *Bull Environ Contam Toxicol* 87:91–95
- Hong Z, Kong M (2003) Issues about recovery of useful minerals contained in tailings. *Min Eng* 1:41–44 (**in Chinese with English Abstract**)
- Irene CMS, Brimhall GH, Alpers CN, Swayze GA (2005) Characterization of waste rock associated with acid drainage at the Penn Mine, California, by ground-based visible to short-wave infrared reflectance spectroscopy assisted by digital mapping. *Chem Geol* 215:453–472
- Jakob S, Gloaguen R, Laukamp C (2016) Remote sensing-based exploration of structurally-related mineralizations around mount Isa, Queensland, Australia. *Remote Sens* 8:358
- Liu Z, Kong F, Liu X, Yang P, Liu X, Wang Y, Pu X (2009a) Suggestions on tailings resources investigation, protection, development and utilization of metal mine in Southeastern Hubei. *Resour Environ Eng* 23:4 (**in Chinese with English Abstract**)
- Liu Z, Liu X, Yang P, Han P, Liu X (2009b) Present status and basic characteristics of tailings accumulation of metal mine in Southeastern Hu Bei. *Min Metal* 18:5–9 (**in Chinese with English Abstract**)
- Liu Z, He H, Liu X, Yang P, Liu X (2010) Preliminary study on material composition of tailings in metal mines, Southeastern Hu Bei Province. *Min Metal* 19:7–12 (**in Chinese with English Abstract**)
- Madani AA (2009) Utilization of Landsat ETM+ data for mapping gossans and iron rich zones exposed at Bahrah area, Western Arabian Shield, Saudi Arabia. *J King Abdulaziz Univ Earth Sci* 20:35–49. <https://doi.org/10.4197/Ear.20-1.3>
- Mars JC, Crowley JK (2003) Mapping mine wastes and analyzing areas affected by selenium-rich water runoff in southeast Idaho using AVIRIS imagery and digital elevation data. *Remote Sens Environ* 84:422–436
- Matar SS, Bamoussa AO (2013) Integration of the ASTER thermal infra-red bands imageries with ecological map of Jabal Al Hasir area, Asir Terrane, the Arabian Shield. *J Taibah Univ Sci* 7:1–7
- Mazhari N, Shafaroudi AM, Ghaderi M (2017) Detecting and mapping different types of iron mineralization in Sangan mining region, NE Iran, using satellite image and airborne geophysical data. *Geosci J* 21(1):137–148
- Mcfeters SK (1996) The use of the Normalized Difference Water Index (NDWI) in the delineation of open water features. *Int J Remote Sens* 17:1425–1432
- Mezned N, Mechrgui N, Abdeljaouad S (2016) Mine wastes environmental impact mapping using Landsat ETM+ and SPOT 5 data fusion in the North of Tunisia. *J India Soc Remote Sens* 44(3):451–455
- Morais MCD (2012) Multi-scale approach using remote sensing images to characterize the iron deposit N1 influence areas in

- Carajás Mineral Province (Brazilian Amazon). *Environ Earth Sci* 66:2085–2096
- Murphy RJ, Monteiro ST (2013) Mapping the distribution of ferric iron minerals on a vertical mine face using derivative analysis of hyperspectral imagery (430–970 nm). *J Photogram Remote Sens* 75:29–39
- Pour AB, Hashim M, Hong JK, Park Y (2017) Lithological and alteration mineral mapping in poorly exposed lithologies using Landsat-8 and ASTER satellite data: North-eastern Graham Land, Antarctic Peninsula. *Ore Geol Rev*. <https://doi.org/10.1016/j.oregeorev.2017.07.018>
- Raj SK, Ahmed SA, Srivatsav SK, Gupta PK (2015) Iron oxides mapping from E0-1 hyperion data. *J Geol Soc India* 86:717–725
- Riaza A, Müller A (2010) Hyperspectral remote sensing monitoring of pyrite mine wastes: a record of climate variability (Pyrite Belt, Spain). *Environ Earth Sci* 61:575–594
- Schimmer R (2008) A remote sensing and GIS method for detecting land surface areas covered by copper mill tailings. In: Pecora 17 – the future of land imaging...going operational, Denver, CO, USA, 18–20 November 2008, pp 1–13
- Shalaby MH, Bishta AZ, Roz ME, El Zalaky MA (2010) Integration of geologic and remote sensing studies for the discovery of uranium mineralization in some granite plutons, Eastern Desert, Egypt. *J King Abdulaziz Univ Earth Sci* 21:1–25. <https://doi.org/10.4197/Ear.21-1.1>
- Shang JL, Morris B, Howarth P, Lévesque J, Staenz K, Neville B (2009) Mapping mine tailing surface mineralogy using hyperspectral remote sensing. *Can J Remote Sens* 35:S126–S141
- Sklute EC, Kashyap S, Dyar MD, Holden JF, Tague T, Wang P, Jaret SJ (2018) Spectral and morphological characteristics of synthetic nanophase iron (oxyhydr)oxides. *Phys Chem Miner* 45:1–26. <https://doi.org/10.1007/s00269-017-0897-y>
- Swayze GA, Smith KS, Clark RN, Sutley SJ, Pearson RM, Vance JS, Hageman PL, Briggs PH, Meier AL, Singleton MJ (2000) Using imaging spectroscopy to map acidic mine waste. *Environ Sci Technol* 34:47–54
- Wang R, Xiong S, Nie H, Liang S, Qi Z, Yang J (2011) Remote sensing technology and its application in geological exploration. *Acta Geol Sin* 85:1699–1743 (in Chinese with English Abstract)
- Xu HQ (2005) A study on information extraction of water body with the modified normalized difference water index (MNDWI). *J Remote Sens* 9:589–594
- Xu HQ, Tang F (2013) Analysis of new characteristics of the first Landsat 8 image and their eco-environmental significance. *Acta Ecol Sin* 33:3249–3257 (in Chinese with English Abstract)
- Zabcic N, Rivard B, Ong C, Mueller A (2014) Using airborne hyperspectral data to characterize the surface pH and mineralogy of pyrite mine tailings. *Int J Appl Earth Obs Geoinf* 32:152–162

Publisher's Note Springer Nature remains neutral with regard to jurisdictional claims in published maps and institutional affiliations.